Hindawi
Shock and Vibration
Volume 2022, Article ID 7109507, 15 pages
https://doi.org/10.1155/2022/7109507

Research Article

Fault Characteristics Analysis of High-Speed Train Transmission Systems

Yang Liu,[1,2] **Zhang Dengbo**,[1] **Yang Yueting**,[3] **and Ruquan Liang**[1]

[1]*School of Mechanical and Vehicle Engineering, Linyi University, Linyi 276000, China*
[2]*School of Mechanical Engineering, Shijiazhuang Tiedao University, Shijiazhuang 050043, China*
[3]*Tengzhou Secondary Vocational Education Center, Tengzhou 277500, China*

Correspondence should be addressed to Yang Liu; yang_8873@126.com

Received 8 July 2022; Revised 3 November 2022; Accepted 9 November 2022; Published 21 November 2022

Academic Editor: Lutz Auersch

The high-speed train speed has a higher requirement for stability and operating safety with its operating speed increasing. The main focus of this paper is on the fault characteristics analysis of a high-speed train transmission system. The governing equation and boundary conditions of the transmission system are derived using the finite element method, in which a Timoshenko beam element is introduced to represent the wheelset shaft, and a rigid mass element is utilized to represent the gears, bearings, and wheels. To investigate the vibration response mechanism of a high-speed train transmission system, the critical speed of the system and its modal response are given. According to the types of high-speed train component fault features, the local fault features of gear, bearing, and wheelset are given. Healthy and faulty systems with localized faults in gear, bearing, and wheelset are studied. The characteristics of amplitude and frequency are verified numerically and the transmission characteristics of signal and relation are explained when there is local fault defect in the system. The results show that under different fault types, the time domain response of the system has obvious periodic impulse response faults, and the fault frequency band characteristic distribution is different in the frequency domain response. The simulation results are consistent with the experimental results.

1. Introduction

The gear bearing wheel is a key component of high-speed train transmission systems. When the vehicles are travelling in a high speed, due to the fault of key components, a high level of vibration and noise may take place. Dynamic analysis of high-speed train transmission systems is the key to researching high-speed train running conditions and fatigue strength under complex excitation. Therefore, understanding how to accurately reveal the dynamic characteristics of the nonlinear high-speed train transmission dynamic model is very much in demand.

Previous investigations on transmission systems and shaft-disk characteristics mainly consisted of two basic methods, namely, the global and local approaches. In the shaft system aspect, Rzadkowski and Maurin [1] introduced a dynamic model of a flexible disk and studied natural frequencies of a rotating shaft-disk system. She et al. [2] investigated the influence of the disk's position and flexibility on the critical speeds and natural frequencies of a coupling shaft-disk-blade unit. Al-Solihat and Behdinan [3] studied the nonlinear dynamic and force transmissibility characteristics of a rotor system supported by a suspension system with nonlinear stiffness and damping. Chiu et al. [4] explored blade-bending, disk-transverse, and shaft-torsion coupling vibration of a flexible shaft-disk system. However, a dynamic model of a rotating system with a beam hypothesis considering gear meshing has been used to explore the systems characterized by gear shaft [5, 6]. Sawalhi and Randall [7] established a modified model for a gearbox by taking into account the gear bearing effect and analyzing the stability of the system. Jianxiong et al. [8] studied the vibration characteristics of gear systems based on a multinode dynamic mode. Hanmant and Pratiher [9] researched the rotor-casing contact phenomena of a large deflection rotor-bearing system under a mass unbalance situation.

The above research mainly focuses on the vibration characteristics of rotors in order to study localized faults in gears. The flexible shaft model can investigate the vibration characteristics of key components. Kahraman et al. [10]used Timoshenko beam theory to propose a gear flexible-shaft dynamic model with consideration of the stiffness of the gear mesh and analyze the dynamics. Later, Kang et al. [11] extended the model to helical gears with the effects of gear eccentricity. Chen et al. [12] studied the critical speed of a gear transmission system using the finite element method. Based on a dynamic model of a wind turbine, Cho et al. [13] analyzed the dynamic behaviors of the gearbox and the natural frequencies of the gearbox. Ma and Xu [14] investigated the accurate calculation of gear stiffness for a nonlinear rotor model.

The literature of bearing dynamics mainly analyzed the dynamic behaviors of the fault bearing. Based on a fault model of the bearing, Harsha et al. [15] analyzed the bearing vibration characteristics caused by the raceway defects. Yang et al. [16] studied the misalignment and contact characteristics of the double-row tapered roller bearing. Furthermore, Yan et al. [17] established a model of a double-row tapered roller bearing that considered elastohydrodynamic lubrication. Recently, Wang et al. [18, 19] investigated the vibration characteristics of axle box bearings under intense wheel-rail excitation. Based on the vehicle-track coupled dynamics model, Huang et al. [20] investigated the fault frequency characteristics of axle box bearings.

As highlighted above, research has addressed the dynamics characteristics of key components of transmission systems. The main objective of this paper is to use the newly developed flexible transmission system dynamics model to investigate the fault characteristics of the key components of the system in a high-speed train. The test experiment is carried out to accurately represent the model by comparing the results from experimental tests and simulations. Based on different bearing, wheel, and gear fault types, the fault characteristics of key components of transmission systems are analyzed theoretically.

2. Dynamic Model

As shown in Figure 1, a high-speed train transmission system is established that takes into account nonlinear factors such as the elastic support of wheel-rails, gear bearings, and flexible shaft elements.

2.1. Rotor-Shaft Element. In finite element analysis, a Timoshenko beam with two nodes is often applied to model a shaft element. A typical element of the shaft is illustrated in Figure 2. Element coordinates of each node is: $(v, w, \varphi, \phi, \theta)$. Considering the lateral bending and torsion deformation, the kinetic energy of the shaft beam element can be written as

$$T^e = \frac{\rho A}{2}\int_0^l \left(\dot{w}^2 + \dot{v}^2\right)\mathrm{d}x + \frac{\rho I_d}{2}\int_0^l \left(\dot{\varphi}^2 + \dot{\phi}^2\right)\mathrm{d}x + \frac{\rho I_o}{2}\left(\Omega + \dot{\theta}_1\right)\int_0^l (\varphi\dot{\phi} - \phi\dot{\varphi})\mathrm{d}x + \frac{\rho I_o}{2}\int_0^l \left(\Omega + \dot{\theta}_1\right)^2 \mathrm{d}x. \tag{1}$$

In the high-speed train transmission system model, the strain potential energy of shaft element is presented as

$$U^{\mathrm{e}} = \frac{1}{2}\iiint_V E\left(-zw'' - yv'' + \frac{1}{2}v' + \frac{1}{2}w'\right)^2 \mathrm{d}V + \frac{\mu AG}{2}\int_0^l \left[(v' - \varphi)^2 + (w' - \phi)^2\right]\mathrm{d}x + \frac{G}{2}\int_0^l I_o(\theta')^2\mathrm{d}x. \tag{2}$$

Here, ρ and A are mass density and cross section area, respectively. μ is the shear factor. E is Young's modulus and G is the shear modulus of rotor material. I_o and I_d are pole moment of inertia and the moment of inertia.

The deformation of the node (v, w) are used to depict the displacements of Z and Y direction, (φ, ϕ) are used to represent the rotational displacements about Z and Y direction, θ is the torsion angle, and then the node function can be written as

$$\{v \;\; w \;\; \varphi \;\; \phi \;\; \theta\}^T = \begin{bmatrix} N_{sl} \\ N \end{bmatrix}\{q(t)\}. \tag{3}$$

Here, $q(t) = (v_1, w_1, \varphi_1, \phi_1, \theta_1, v_2, w_2, \varphi_2, \phi_2, \theta_2)$ is displacement vector of element node. The spatial constraint matrices $[N_{s1}]$ and $[N]$ can be written as

$$[N_{s1}] = \begin{bmatrix} N_{s1} & 0 & 0 & N_{s2} & 0 & N_{s3} & 0 & 0 & N_{s4} & 0 \\ 0 & N_{s1} & -N_{s2} & 0 & 0 & 0 & N_{s3} & -N_{s4} & 0 & 0 \end{bmatrix}, \tag{4}$$

$$[N] = \begin{bmatrix} 0 & -N_{t1} & N_{t2} & 0 & 0 & 0 & -N_{t3} & N_{t4} & 0 & 0 \\ N_{t1} & 0 & 0 & N_{t2} & 0 & N_{t3} & 0 & 0 & N_{t4} & 0 \\ 0 & 0 & 0 & 0 & N_{\mathrm{r}3} & 0 & 0 & 0 & 0 & N_{\mathrm{r}4} \end{bmatrix}, \tag{5}$$

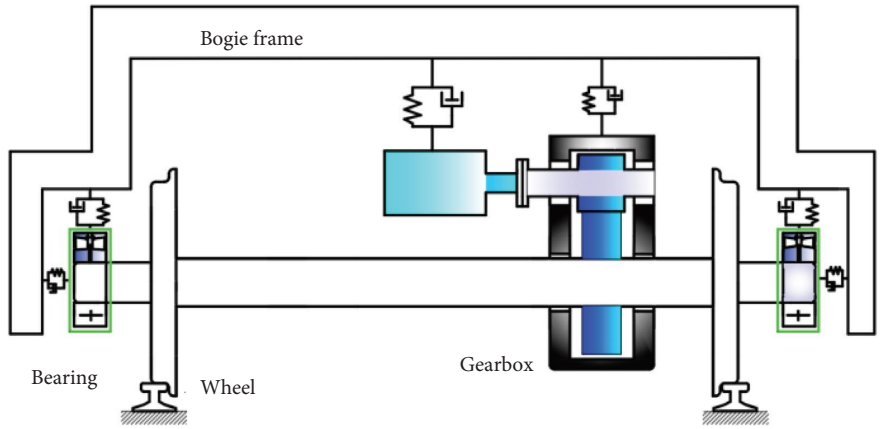

Figure 1: High-speed train transmission system.

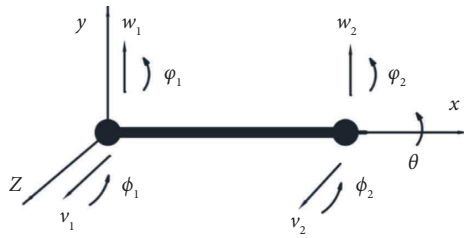

Figure 2: Timoshenko beam shaft model.

where $[N_{si}]$ and $[N_{ti}]$ are the shape functions of the shaft element [12].

Substituting the above equation (1)–(5) into the Lagrange equation,

$$\frac{d}{dt}\left(\frac{\partial L}{\partial \dot{q}_i}\right) - \frac{\partial L}{\partial q_i} = Q_i, \tag{6}$$

where Q_i is the external force, $L = T - U$. The dynamics equation of shaft beam element is represented as

$$[M]_s\ddot{q} + \Omega[G]_s\dot{q} + [K]_s q = 0, \tag{7}$$

where Ω is the spin speed of the shaft.

2.2. Meshing Gear Element Model. The model of meshing gear is shown in Figure 3. The node coordinates of meshing gear are $(v_{ci}, w_{ci}, \varphi_{ci}, \phi_{ci}, \theta_{ci}, i = 1, 2)$. Kinetic energy of meshing gear is described as

$$\begin{aligned} T_c = {} & \frac{1}{2}m_{ci}\left(\dot{v}_{ci}^{\,2} + \dot{w}_{ci}^{\,2}\right) + \frac{1}{2}I_{dc\,i}\left(\dot{\varphi}_{ci}^{\,2} + \dot{\phi}_{ci}^{\,2}\right) \\ & + \frac{I_{oci}}{2}\left(\Omega + \dot{\theta}_{ci}\right)\left(\varphi_{ci}\dot{\phi}_{ci} - \phi_{ci}\dot{\varphi}_{ci}\right) + \frac{I_{oci}}{2}\left(\Omega + \dot{\theta}_{ci}\right)^2. \end{aligned} \tag{8}$$

Considering the effect of backlash, the potential energy of meshing gear element is given as

$$\begin{aligned} U_c = {} & \frac{1}{2}k_m(t)\left(w_{c1} - w_{c2} + \theta_{c1}r_1 - \theta_{c2}r_2 - e\right)^2 \\ & + \frac{1}{2}K_i\left(w_{c1} - w_{c2}\right)^2 + \frac{1}{2}C_i\left(\dot{w}_{c1} - \dot{w}_{c2}\right)^2 \\ & + \frac{1}{2}c_{\mathrm{m}}\left(\dot{w}_{c1} - \dot{w}_{c2} + \dot{\theta}_{c1}r_1 - \dot{\theta}_{c2}r_2 - \dot{e}\right)^2. \end{aligned} \tag{9}$$

The influence of gear eccentric force on meshing gear element can be expressed as

$$W_c = m_{ci}r_i\Omega^2\left(w_{ci}\cos\Omega t + v_{ci}\sin\Omega t\right) + T_i\theta_{ci}. \tag{10}$$

Here, $k_m(t)$ is the time-varying meshing stiffness of gears. c_m is the comprehensive damping coefficient of gear meshing [12]. r_1 and r_2, respectively, denote the radial of base circles of the driving gear and the driven gear. $I_{dc\,i}$ denotes the moment of inertia of the meshing gear. m_{ci} denotes the mass of meshing gear. K_i and C_i are the elastic stiffness and elastic damping, respectively. T_i $(i = 1, 2)$ is the torque of input and output.

Using the Lagrange approach to (6), the motion equation of meshing gear element is given as

$$[M]_g\ddot{q}^c + \left([C]_g + \Omega[G]_g\right)\dot{q}^c + [K]_g q^c = [Q], \tag{11}$$

where $[M]_g$, $[C]_g$, $[G]_g$, and $[K]_g$ are the mass matrix of meshing gear element, the damping matrix, the gyroscopic matrix, and the time-varying stiffness matrix, respectively.

2.3. Bearing Element Model. Ignoring the axial force and the lateral motion and considering the normal contact force, the supporting bearing element model of tapered roller bearings is shown in Figure 4. Bearing element is assumed as a nonlinear contact. The contact force and moments between the roller and inner raceway can be described according to the Hertzian line of contact

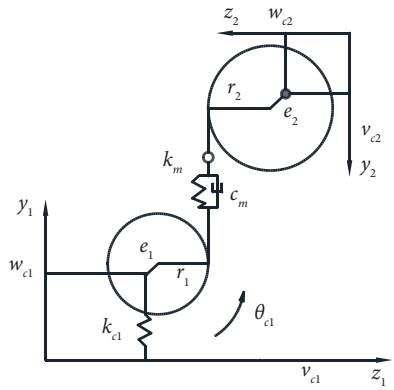

Figure 3: Meshing gear element model.

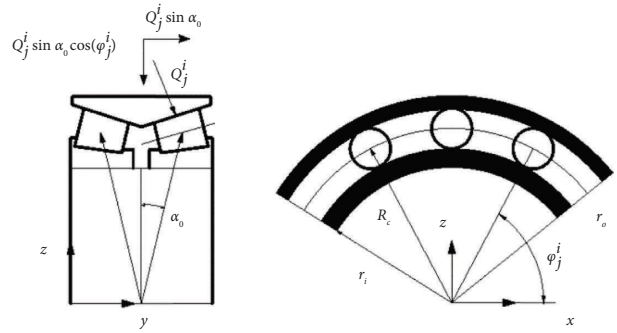

Figure 4: Bearing contact element model.

$$F_{BN} = \begin{Bmatrix} F_{yb} \\ F_{zb} \end{Bmatrix} = \sum_{i=1}^{2} \sum_{j=1}^{N} Q_j^i \begin{Bmatrix} \cos(\alpha_0)\cos(\phi_j^i) \\ \cos(\alpha_0)\sin(\phi_j^i) \end{Bmatrix}, \tag{12}$$

$$M_{BN} = \begin{Bmatrix} M_{xb} \\ M_{yb} \\ M_{zb} \end{Bmatrix} = \sum_{i=1}^{2} \sum_{j=1}^{N} Q_j^i \begin{Bmatrix} 0 \\ R_c \sin(\phi_j^i) \\ -R_c \cos(\phi_j^i) \end{Bmatrix}, \tag{13}$$

where Q_j^i is the Hertz contact normal force. α_0 is the unloaded contact angle. R_c is the radius of bearing. $\phi_j^i = \Omega t + 2\pi(j-1)/N$ denotes the race contact angle of the j-the rolling element.

Bearing contact element coordinates are $(v_{bi}, w_{bi}, \varphi_{bi}, \phi_{bi}, \theta_{bi})\ i = 1, 2$. Applying the Lagrange method, the motion equation of bearing contact element can be obtained as

$$[M]_b \ddot{q}^b + ([C]_b)\dot{q}^b + [K]_b q^b = [F]^b, \tag{14}$$

where $[M]_b$, $[C]_b$, $[K]_b$, and $[F]_b$ are mass matrix of bearing elements, damping matrix, stiffness matrix, and contact force matrix, respectively.

2.4. Wheel Element Model. In Figure 5, the coordinates of the wheel element are $(v_{li}, w_{li}, \varphi_{li}, \phi_{li}, \theta_{li}, i = 1, 2)$. The kinetic energy and the potential energy of wheel can be expressed as

$$T_l = \frac{1}{2} M_{li}\left(\dot{v}_{li}^{\,2} + \dot{w}_{li}^{\,2}\right) + \frac{1}{2} I_{dc\,i}\left(\dot{\varphi}_{li}^{\,2} + \dot{\phi}_{li}^{\,2}\right) + \frac{I_{oli}}{2}\left(\Omega + \dot{\theta}_{li}\right)\left(\varphi_{li}\dot{\phi}_{li} - \phi_{li}\dot{\varphi}_{li}\right) + \frac{I_{oli}}{2}\left(\Omega + \dot{\theta}_{li}\right)^2, \tag{15}$$

$$U_1 = \frac{1}{2} K_{li}(w_{li})^2 + \frac{1}{2} C_{li}(\dot{w}_{li})^2. \tag{16}$$

By using the Lagrange method, the motion equation of wheel-rail element can be written as

$$[M]_w \ddot{q}^w + ([C]_w + \Omega[G]_w)\dot{q}^w + [K]_w q^w = [F]. \tag{17}$$

where $[M]_w$, $[C]_w$, $[G]_w$, and $[K]_w$ denote the mass matrix, the damping matrix, the gyroscopic matrix contact force matrix, and the support stiffness matrix, respectively, of the wheel-rail element [18].

2.5. Equation of the High-Speed Train Transmission System. Considering the above factors, substituting equations (11)–(17) into (7), the equation of high-speed train transmission system can be expressed as

$$[M]\ddot{q} + ([C] + \Omega[G])\dot{q} + [K]q = [Q], \tag{18}$$

where $\{q\} = [v_1, w_1, \varphi_1, \phi_1, \theta_1, \ldots\ldots, \theta_n]^T$, n denotes the number of nodes. $[M]$, $[C]$, $[G]$, and $[K]$ are the mass matrix, the damping matrix, the gyroscopic matrix, and the

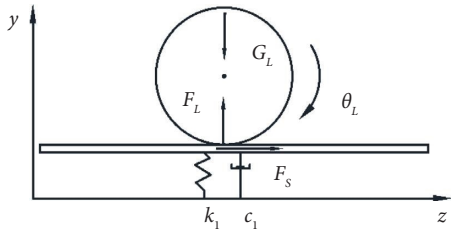

Figure 5: Wheel-rail contact model.

stiffness matrix, respectively, of the high-speed train transmission system.

3. Natural Frequency and Modal Functions

When the high-speed train transmission system is subjected to bending and torsion vibration, the homogeneous equation of rotor system can be presented as

$$[M]\ddot{q} + ([C] + \Omega[G])\dot{q} + [K]q = 0. \tag{19}$$

In order to find the critical speed of the equation, the equation can be transformed into a linear equation

$$[A]\dot{\Psi} + [\mathrm{B}]\Psi = 0, \tag{20}$$

where

$$\Psi = \begin{bmatrix} \dot{q} \\ q \end{bmatrix},$$
$$[A] = \begin{bmatrix} 0 & -[M] \\ [M] & [C] \end{bmatrix}, \tag{21}$$
$$[\mathrm{B}] = \begin{bmatrix} [M] & 0 \\ 0 & [K] \end{bmatrix}.$$

Calculating the response characteristics of the system under different rotating speeds, the train transmission systems can be obtained from the Campbell diagram. When the speed of rotation Ω is equal to eigenvalue λ, the critical speed of the transmission system is obtained, as shown in Figure 6. From the calculated Campbell diagram results, it can be seen that part of the natural frequencies change obviously with the increase of the speed, while the other part of the natural frequencies is basically not affected by the speed.

When the rotor speed changes, the value of the first five-order natural frequencies of the rotor system is obtained in Table 1.

The first-to-third-order mode of the high-speed train system is shown in Figure 7. The vibration amplitude of the mode shapes of the driving shaft changes little, and the vibration amplitude of the driven shaft changes obviously in Figures 7(a) and 7(b). The vibration of the driving shaft is large in Figure 7(c). Under the low-order mode of the system, the vibration amplitude of the driven shaft is more important. In the high-order mode of the system, the vibration amplitude of the driving shaft is especially important.

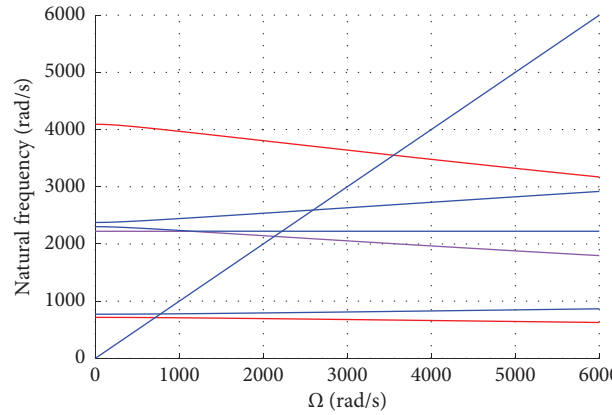

Figure 6: Critical rotor speed.

Table 1: Natural frequency.

Model	First	Second	Third	Fourth	Fifth
ω rad/s	691.3	776.6	1855.56	2221.6	2259.45

4. Fault Feature of Gear Bearing Wheel

4.1. Fault Feature of Gear with Tooth Root Crack. In order to study the fault characteristics of key components of the transmission system, the stress characteristics of key components must be considered. In the gear meshing element, the change in gear contact stiffness can effectively reflect the vibration characteristics of the gear system. The energy method [19] is used in this paper. The total potential energy was assumed to include four components: hertz energy U_h, bending energy U_b, shear energy U_a, and axial compressive energy U_s. The total potential energy can be expressed as follows:

$$U_h = \frac{F^2}{2K_h},$$
$$U_b = \frac{F^2}{2K_h} = \int_0^d \frac{M^2}{2EI_x}\mathrm{d}x,$$
$$U_a = \frac{F^2}{2K_a} = \int_0^d \frac{1.2{F_b}^2}{2GA_x}\mathrm{d}x, \tag{22}$$
$$U_s = \frac{F^2}{2K_s} = \int_0^d \frac{F_a^2}{2EA_x}\mathrm{d}x,$$
$$I_x = \frac{2}{3}{h_x}^3 L, A_x = 2h_x L,$$

where F is the meshing force. F_b and F_a are the radial and tangential forces, respectively. G and E represent Young's modulus and shear modulus, respectively. L is the width of tooth. When gears are meshing, the time-varying stiffness can be obtained by

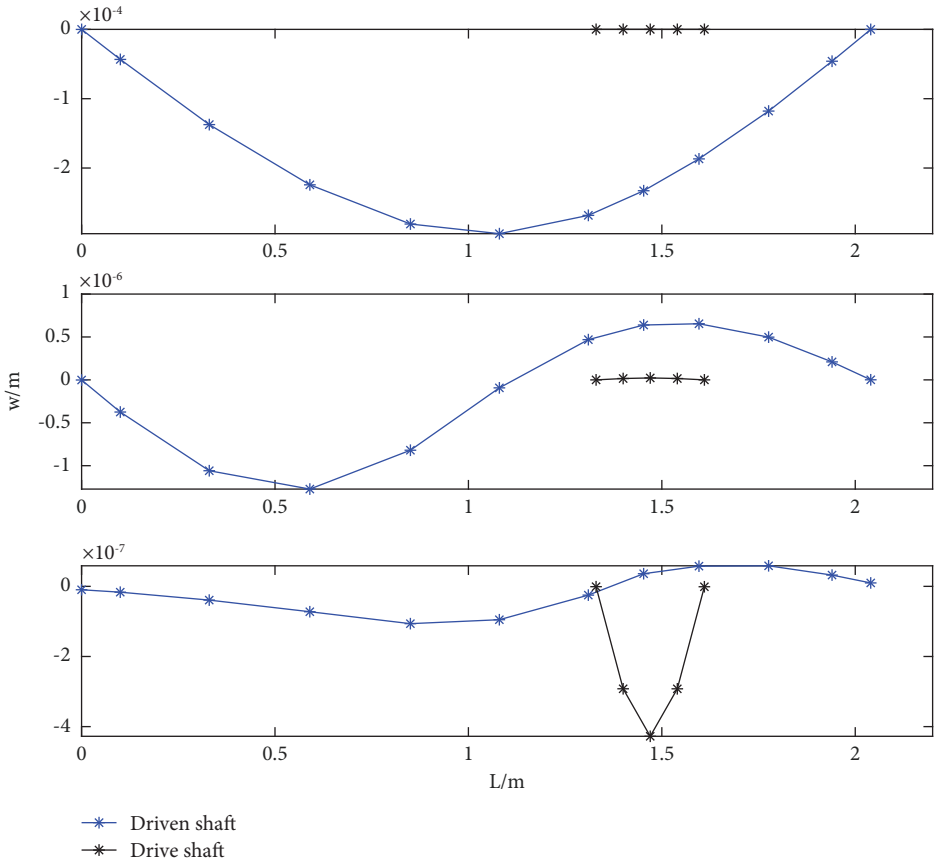

Figure 7: First-to-third-order modal analysis.

$$K_m = \frac{1}{\left(1/K_h + 1/K_{b1} + 1/K_{s1} + 1/K_{f1} + 1/K_{a1} + 1/K_{b2} + 1/K_{s2} + 1/K_{a2} + 1/K_{f2}\right)}, \tag{23}$$

where K_h, K_b, K_s, and K_a represent the Hertzian, bending, shear, and axial compressive mesh stiffness, respectively [20].

When the gear root crack occurs, it causes a change in the bending deformation stiffness and shear deformation stiffness of the gear tooth. The crack length $q = 2$ mm. The calculating formula for the moment of inertia is shown in Figure 8, and the section area is as follows:

$$I_{xc} = \begin{cases} \dfrac{1}{12}(h_c + h_x)^3 L, x \le g_c, \\ \dfrac{1}{12}(2h_x)^3 L, x > g_c, \end{cases} \quad A_{xc} = \begin{cases} (h_c + h_x)L, x \le g_c, \\ 2h_x L, x > g_c, \end{cases} \tag{24}$$

where L is the length of contact. h_x is the distance between the meshing point of the gear tooth profile and the middle line of the gear tooth. h_c is the height of the gear crack to the midline.

4.2. Fault Feature of Gear with Surface Wear. As shown in Figure 9, when the gear surface wears, the formula of moment of inertia and section area of the gear is described as

$$I_{xc} = \begin{cases} \dfrac{1}{12}(2h_x)^3 L - \left(h_d^3 l_d\right), \text{for fault region}, \\ \dfrac{1}{12}(2h_x)^3 L, \text{for healthy region}, \end{cases} \tag{25}$$

$$A_{xc} = \begin{cases} 2h_x L - h_d l_d, \text{for fault region}, \\ 2h_x L, \text{for healthy region}, \end{cases}$$

where l_d and h_d are shown in Figure 9. Other parameters are detailed in reference [21].

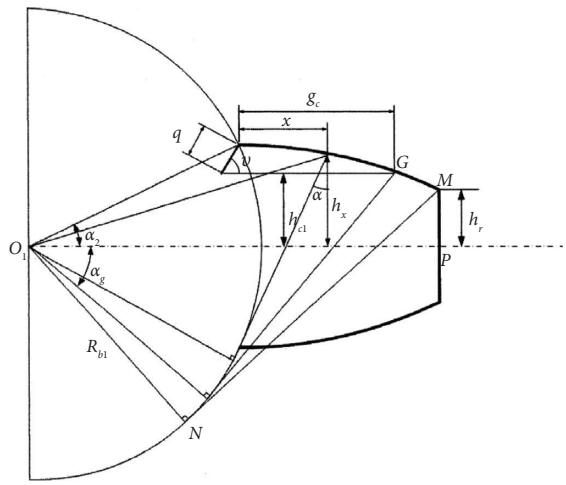

Figure 8: Modeling of a gear tooth crack.

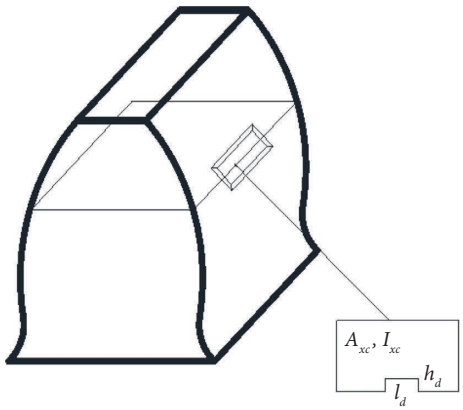

Figure 9: Schematic diagram for spalled gear tooth.

4.3. Bearing Outer Race Defect. As shown in Figure 10, a local fault is considered as a small rectangular spall in the outer race. The position angle of defect is θ_d. The central angle of the defect is θ_o. The defect width is B = 1mm. The radius of the cylinder roller is R_z. When the rolling body passes through the fault region, the normal displacement is λ. The displacement can be expressed as

$$\lambda = \begin{cases} R_z - \sqrt{R_z^2 - (B/2)^2}, \theta_d < \mod(\theta_i, 2\pi) < \theta_d + \theta_o, \\ 0, \text{else}. \end{cases} \tag{26}$$

When the tapered roller is in the defect region, the contact deformation of tapered roller can be formulated as

$$\delta_{\mathrm{d}} = v_i \cos\theta_i + w_i \sin\theta_i - \gamma_0 - \lambda, \tag{27}$$

where $\theta_i = \omega_c t + 2\pi(i-1)/N$. N, γ_0 are the number of roller and bearing clearance. The angular velocity of the cage is ω_{c} [5].

4.4. Bearing Inner Race Fault. As shown in Figure 11, a local fault is considered as a small rectangular spall in the inner race. θ_{d1} and θ_{c} are initial position angle and the central angle of the defect, respectively. The defect width is B_1 = 1mm. When the rolling body passes through inner fault region, the contact displacement is λ_{i}. The displacement can be expressed as

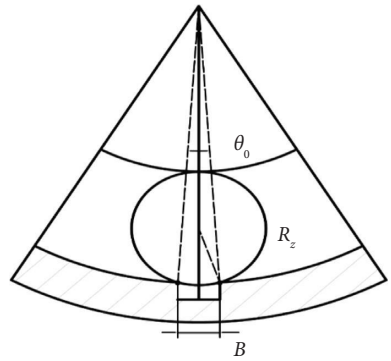

Figure 10: Outer race defect.

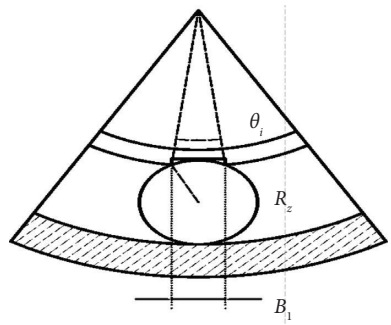

Figure 11: Inner race defect.

$$\lambda_{\mathrm{i}} = \begin{cases} R_z - \sqrt{R_z^2 - (B_1/2)^2}, & \theta_{d1} < \mod(\theta_j, 2\pi) < \theta_{d1} + \theta_{\mathrm{c}}, \\ 0, & \text{else}. \end{cases} \tag{28}$$

When the tapered roller is in the fault region, the contact deformation of cylinder roller can be formulated as

$$\delta_{\mathrm{d}} = v_i \cos\theta_{\mathrm{j}} + w_i \sin\theta_{\mathrm{j}} - \gamma_0 - \lambda_i, \tag{29}$$

where $\theta_{\mathrm{j}} = (\omega_r - \omega_c)t + 2\pi(j-1)/N$. The angular velocity of rotor is ω_{r}.

4.5. Polygonal of Wheels Fault. The extreme running conditions of high-speed trains often cause wheel deformation. As shown in Figure 12, the fault feature of the wheel surface deformation is considered a wheel polygonal with harmonic curve. The expression of surface deformation is as follows:

$$\begin{cases} \Delta R(\omega t) = \sum_i^n A_i \sin(n\omega t + \varphi_o), R(\omega t) = R - \Delta R(\omega t), \end{cases} \tag{30}$$

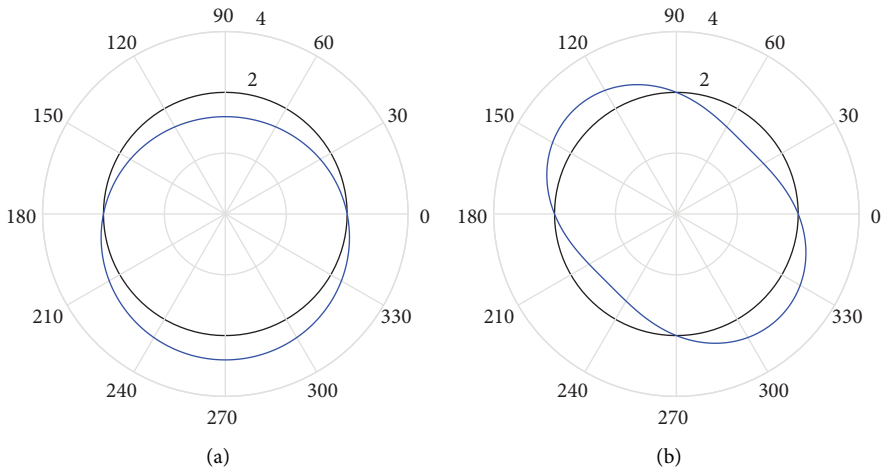

Figure 12: The first-second order of the wheel is not round.

where the angle φ_0 is the initial phase. Wheel Angle is ω. The ripple amplitude of the wheel is ΔR.The radius of the wheel is R.

When the wheel experiences polygonal wear, the expression of the displacement relation between the wheel node and surface deformation is as follows:

$$\left\{\Delta q_1^l\right\} = [T_i]\left\{q_i^l\right\} + \{\Delta R\}, \tag{31}$$

where the coordinates of the wheel is q_i^l, wheel-rail contact angle β_o, transfer matrix T_i is as follows:

$$[T_1]\begin{bmatrix} \cos\varphi_l & -\sin\varphi_l & & & \\ \sin(\beta_0+\phi_l) & \cos(\beta_0+\phi_l)\cos\varphi_l & & & \\ & & 1 & & \\ & & & 1 & \\ & & & & 1 \end{bmatrix}. \tag{32}$$

5. Dynamic Simulation Analysis

In this paper, high-speed train transmission system is taken as the research object. Given system parameters, the length of the supporting shaft is L = 1440mm. The outside diameter of shaft section is r = 65mm. The quality of the wheels is m = 305kg. The mass of concentrated inertia is I_{o1} = 18.75kg.m^2. The numbers of teeth are z_1 = 14, z_2 = 63, respectively. The module of gear is m_a = 6mm. The width of teeth is B_g = 90cm. The driven shaft bearing is NJ2232. The number of rollers is N = 17, r_i, r_o are the inner and outer race radius of the bearing. The pitch diameter of the bearing is D = 380mm and the ball diameter d = 34mm. The drive shaft speeding is n_1 = 1600r/ min. Table 2 shows the parameters of the system. Table 3 shows the bearing gear fault parameters.

5.1. Normal System Response. Figure 13 shows the time domain waveform and frequency spectrum of vertical response of the driven gear nodes. Under the influence of time-varying meshing stiffness, time history response shows that the amplitude of acceleration of driven gear has obvious gear meshing periodic T_m, as shown in Figure 13(a). Spectral response shows that FFT power density of acceleration of driven gear has clear gear meshing frequency f_m, $2f_m$, and frequency doubling, as shown in Figure 13(b).

Table 2: Parameters of the system.

Parameter	Value (Hz)
Drive shaft frequency	$f_2 = 5.9$
Gear meshing frequency	$f_m = f_1 z_1 = f_2 z_2 = 374$
Bearing cage frequency	$f_c = f_2\ (r_i/r_o + r_i) = 2.17$
Bearing outer frequency	$f_o = 0.5 f_r\ (1 - \mathrm{dcosa}/D)N = 37$
Bearing inner frequency	$f_i = 0.5 f_r\ (1 + \mathrm{dcosa}/D)N = 63.1$

Table 3: Parameters of the fault.

Fault type	Size (mm)
Gear root crack length	$L = 0.5$
Gear wear width and length	$B = 0.5$; $L = 1$
Bearing outer fault width	$B = 1$
Bearing inner fault width	$B = 1$

5.2. System Response under Gear Root Crack. During the driving gear occurs root crack, the time domain waveform and frequency spectrum of driven gear nodes are shown in Figure 14. The time domain response has an obvious period T_s, as shown in Figure 14(a), which is the rotating period of the crack gear. In the spectrum, some new frequency components appear around the natural and meshing frequencies. The gear fault frequency f_s is mainly concentrated in the gear meshing frequency band, as shown in Figure 14(b).

5.3. System Response under Gear Wear. During the surface of the driving gear is slightly worn, the time domain waveform and frequency spectrum of vertical response of the driven gear nodes are shown in Figure 15. The system has obvious

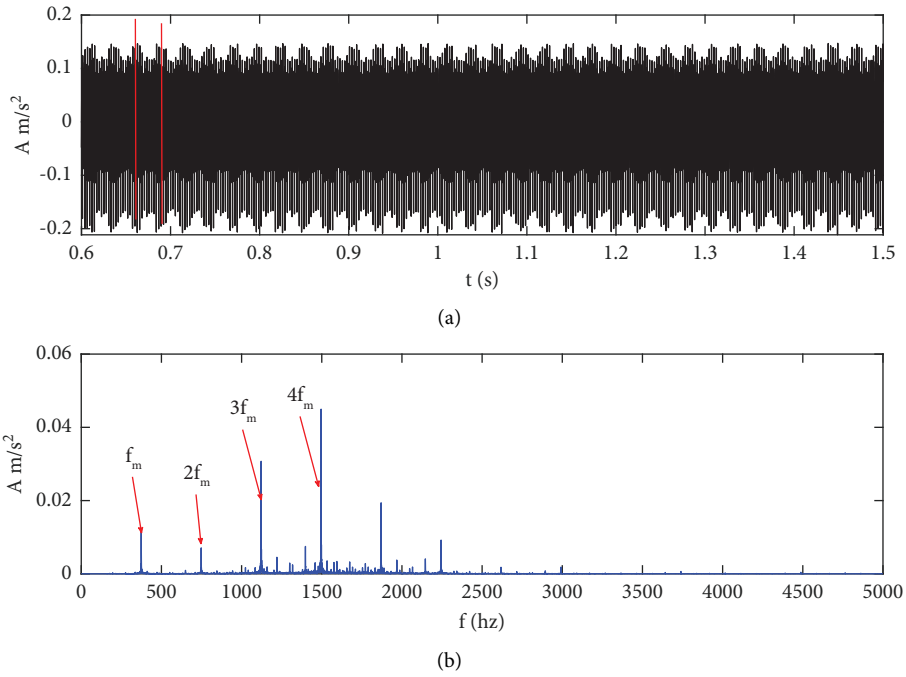

Figure 13: Responses of the driven gear node: (a) the time domain; (b) the frequency domain.

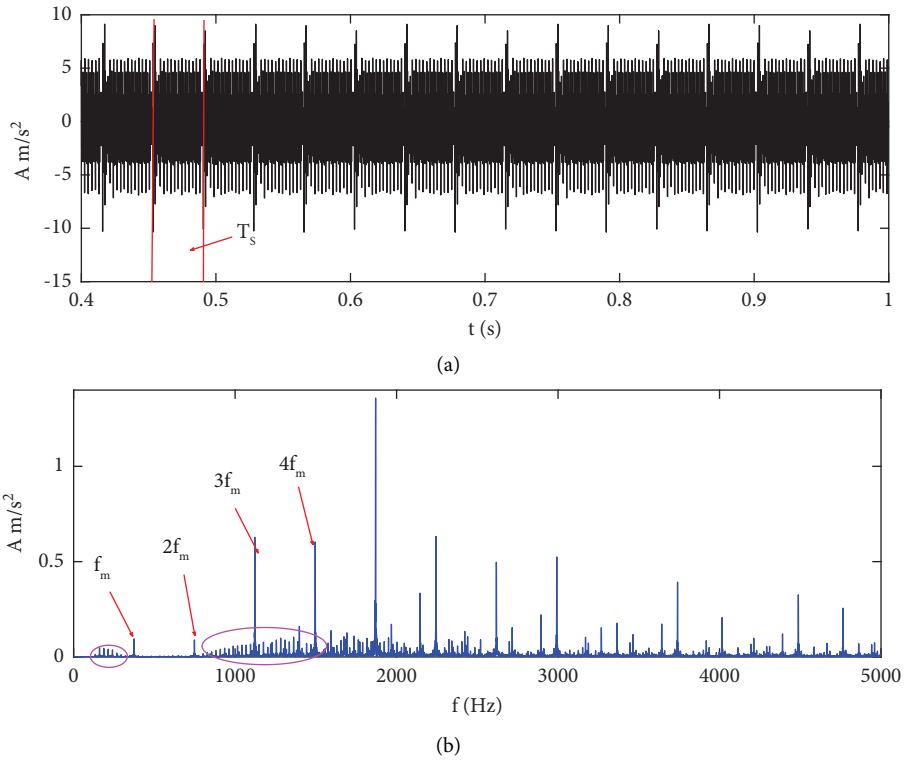

Figure 14: Responses of driven gear node: (a) the time domain; (b) the frequency domain.

periodic impact response of gear in time domain response. T_s is the rotation period of worn gear shaft. The vibration amplitude of vertical response of the driven gear nodes increased in Figure 15(a). From the spectrum shown in Figure 15(b), the meshing frequency f_m and the corresponding components of the doubling frequency $3f_m$ can be clearly found. Moreover, the gear fault frequency is mainly concentrated in the gear meshing frequency band.

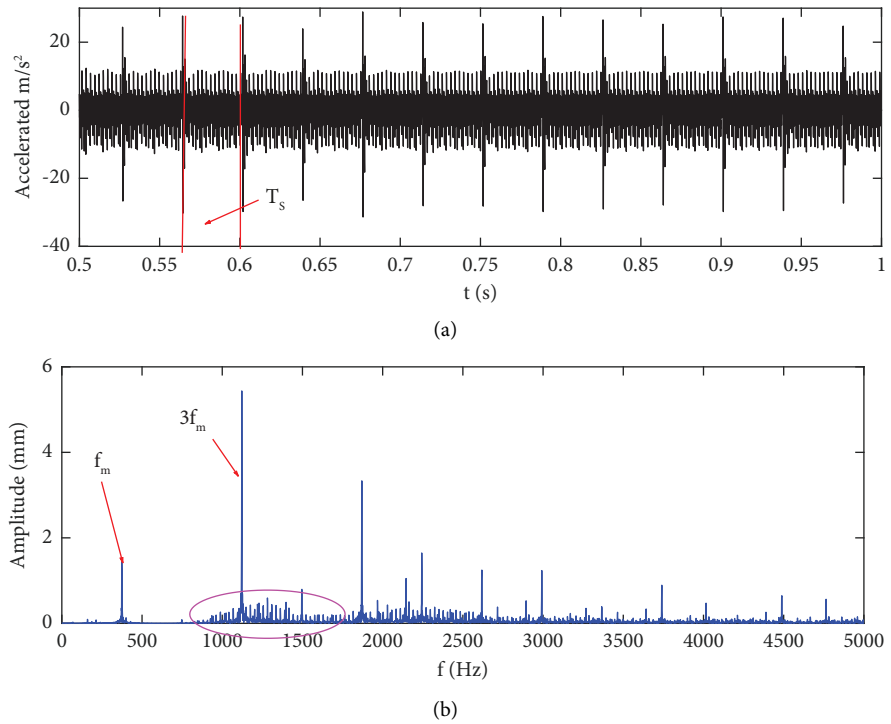

Figure 15: Responses of driven gear node: (a) the time domain; (b) the frequency domain.

5.4. Bearing Outer Race Response. During the outer race of the driven shaft bearing has local fault, the time domain waveform and frequency spectrum of vertical response of the fault bearing nodes are shown in Figure 16. The time domain response of the system has periodic impulse response, as shown in Figure 16(a). T_o is period of fault bearing outer ring. From the spectrum shown in Figure 16(b), there are bearing fault frequencies f_o. Moreover, the bearing fault frequency is mainly concentrated in the high frequency of the system.

5.5. Bearing Inner Race Response. During the inner race of the driven shaft bearing has local fault, the time domain waveform and frequency spectrum of the fault bearing nodes are shown in Figure 17. T_i is the inner race rotation period of the fault bearing, as shown in Figure 17(a). From the spectrum shown in Figure 17(b), there are obvious frequencies of bearing fault f_i. The bearing fault frequency also is mainly concentrated in the high frequency of the system.

5.6. Polygonal Wear of Wheels Response. When the left wheel of driven has $N = 2$ polygonal wear, the time domain waveform and frequency spectrum of the wheel node are shown in Figure 18. According to the time domain waveform shown in Figure 18(a), under the influence of wheel polygonal wear, time domain response has a period of $0.5T_2$ of strong impact. From the spectrum shown in Figure 18(b), there are $2f_2$ of driven shaft. When the wheel has local fault, the fault feature frequency is mainly affected by the different orders of the polygon and the response feature frequency is $N \times f_2$. The fault feature is mainly distributed in the low-frequency band.

5.7. Couple Fault Response. During the outer ring of the left axle box bearing, the driving gear and the wheel have local fault, the vertical vibration response of the fault bearing node are shown in Figure 19. According to the time domain waveform shown in Figure 19(a), there is an obvious impulse response T_2 caused by a wheel fault. Compared with wheel fault, gear and bearing fault response is not obvious. Figure 19(b) shows the spectrum diagram. Local figure is shown in Figure 19(b) (part enlarge A), it has obvious wheel fault frequency f_2 in the whole frequency band. Local figure is shown in Figure 19(b) (part enlarge B), the mesh frequency f_m and the gear fault frequency f_s is apparent. The local figure is shown in Figure 19(b) (part enlarge C), and the bearing fault frequency f_o is apparent and distributed in the high frequency band.

5.8. Comparison of Simulation Experiments. The long-term tracking experiments of Fuxing Hao are presented in Figure 20. When the train is running at speed $n_1 = 3200$ r/min, the vibration response of the bearing axle box is presented in Figure 21. Under the influence of the running environment, there are no periodic response characteristics in the time-frequency response in Figure 21(a). The acceleration response of the axle box is very small because the wheel-rail interference excitation is small in the early stages. In addition, there are obvious gear meshing frequencies and multiple frequency characteristics in the frequency response in Figure 21(b).

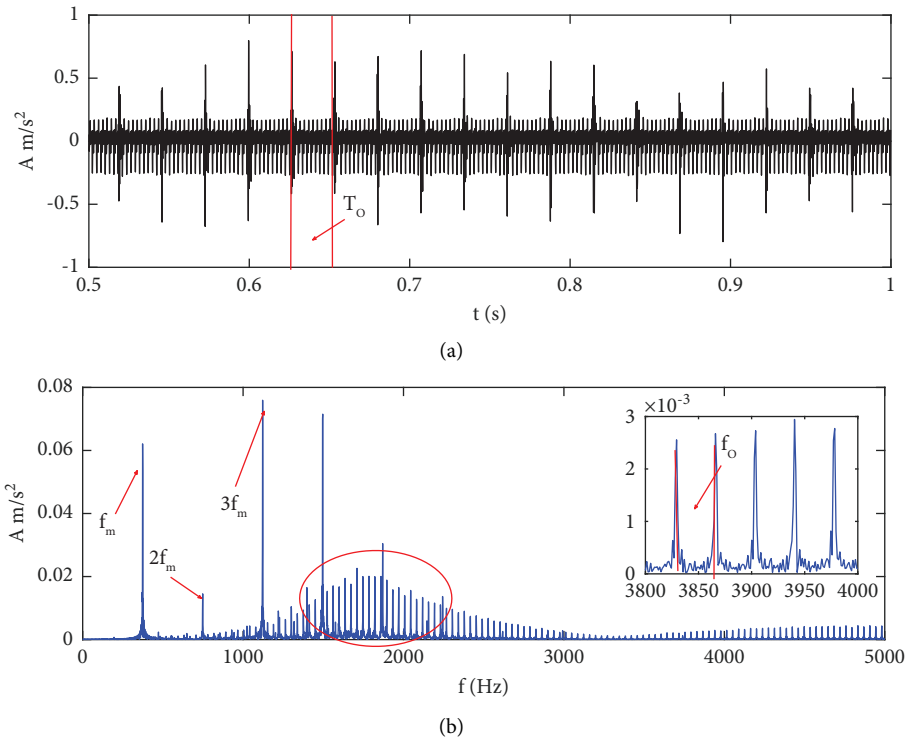

Figure 16: The responses of the bearing node of the driven shaft with outer fault: (a) the time domain; (b) the frequency domain.

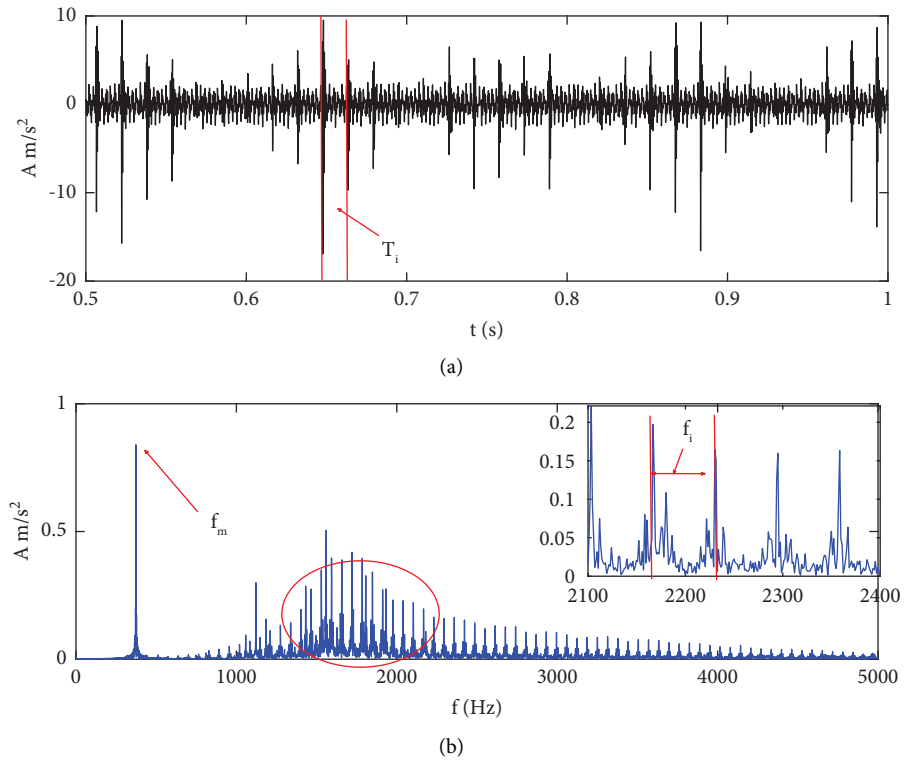

Figure 17: The response of the bearing node of the driven shaft with inner fault: (a) the time domain; (b) the frequency domain.

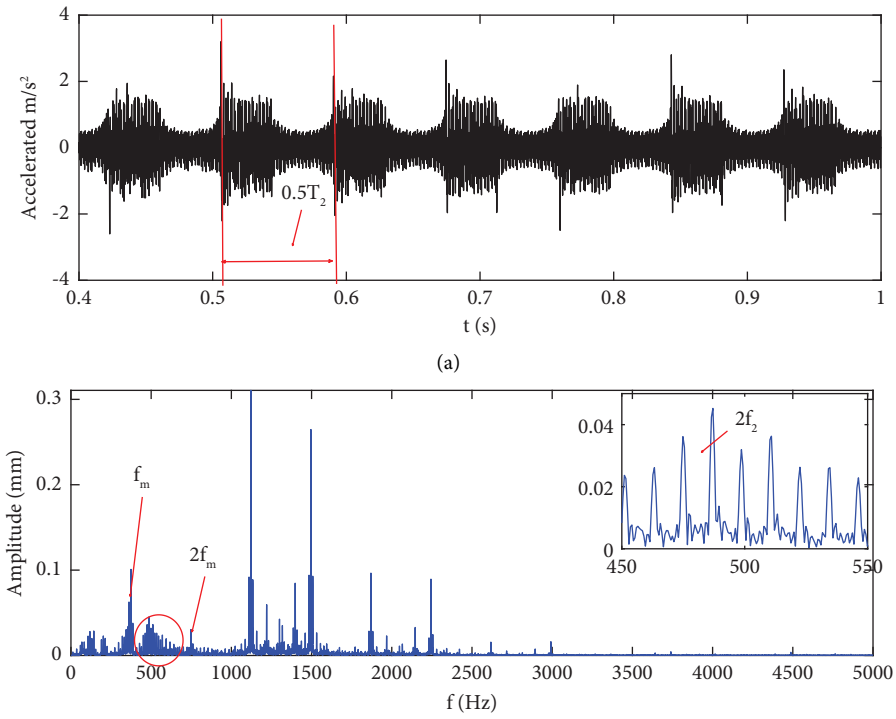

Figure 18: The responses of the wheel node of the driven shaft with polygon fault: (a) the time domain; (b) the frequency domain.

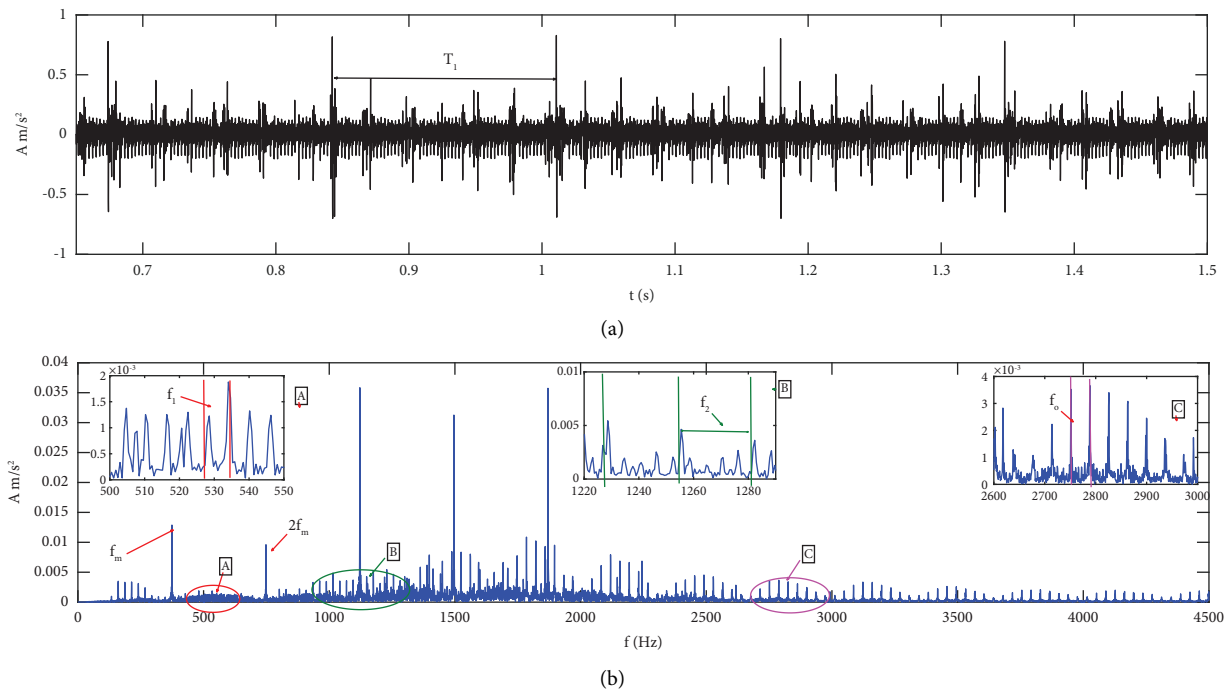

Figure 19: The responses of the bearing node of the driven shaft with couple fault: (a) the time domain; (b) the frequency domain.

Specifically, the simulation signals are basically the same as the vibration response characteristics.

The vertical vibration responses of the bearing node without fault are shown in Figure 22. Compared to the experimental data, the acceleration response of the bearing is basically consistent, as shown in Figure 22(a). In addition, there are obvious gear meshing frequencies and multiple

Figure 20: The long-term tracking test of Fuxing Hao.

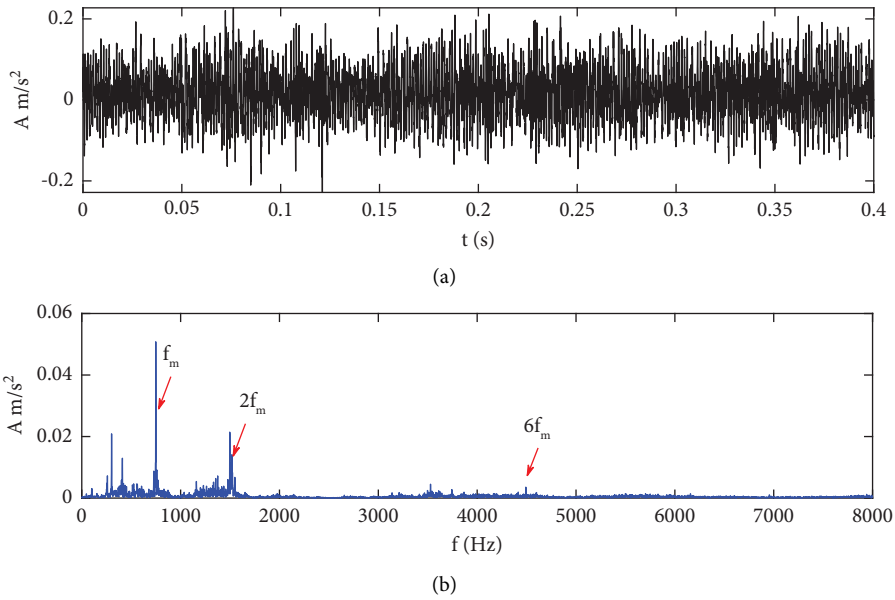

Figure 21: Responses of driving bearing node: (a) the time domain; (b) the frequency domain.

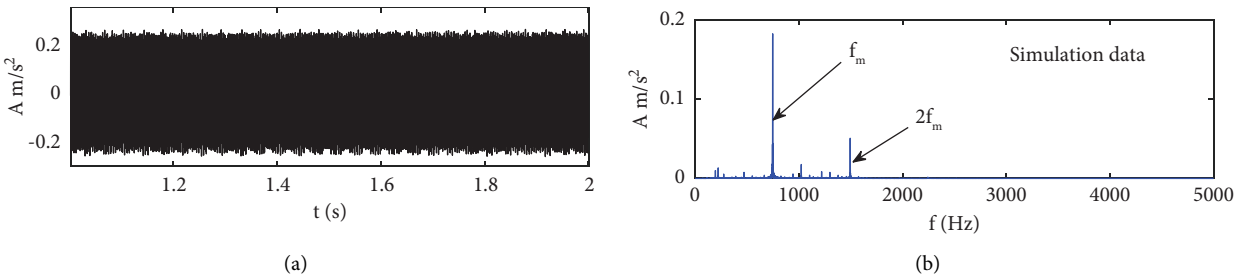

Figure 22: The responses of the bearing node of the driven shaft: (a) the time domain; (b) the frequency domain.

frequency characteristics in the frequency response, as shown in Figure 22(a).

6. Conclusion

In this paper, the kinematic model of a high-speed train transmission system is established, and the fault characteristics of the bearing, wheel, and gear elements are studied.

The dynamic model of the system is established, which can better analyze the transmission relationship and the influence between bearings, wheels, and gears. The change in system response caused by faults in bearings, wheels, and gears is studied. When there is a gear fault, the vibration energy of the system of rotors is distributed in the low resonance frequency band. At the same time, the gear meshing frequency band has an obvious modulation phenomenon. When there is a bearing fault, the vibration energy of the rotor system is distributed in the high resonance frequency band. When the wheel is subject to polygonal wear, the fault feature frequency is mainly affected by the different orders of the polygon, and the response feature frequency is $N \times f_2$. The fault feature is mainly distributed in the low-frequency band. When the system is couple fault, the impact caused by wheel fault is obvious. However, the frequency band position of each component of the system has not changed.

In the low-order mode of the system, the vibration amplitude of the driven shaft is more important. In the high-order mode of the system, the vibration amplitude of the driving shaft is especially important.

Data Availability

No data were used to support this study.

Conflicts of Interest

The authors declare that they have no conflicts of interest.

Acknowledgments

This study was financially supported by the National Natural Science Foundation of China (grant nos. 12002142 and 51976087) and the National Natural Science Foundation of Shandong Province (grant nos. ZR202102180973 and ZR202102230860).

References

[1] R. Rzadkowski and A. Maurin, "Multistage Coupling of eight mistuned bladed discs on a solid shaft of the steam turbine, forced vibration analysis," *Journal of Vibration Engineering and Technologies*, vol. 26, no. 1, pp. 495–508, 2014.

[2] H. She, C. Li, Q. Tang, and B. Wen, "Influence mechanism of disk position and flexibility on natural frequencies and critical speeds of a shaft-disk-blade unit," *Journal of Sound and Vibration*, vol. 469, no. 21, pp. 115156–120, 2020.

[3] M. K. Al-Solihat and K. Behdinan, "Nonlinear dynamic response and transmissibility of a flexible rotor system mounted on viscoelastic elements," *Nonlinear Dynamics*, vol. 97, no. 2, pp. 1581–1600, 2019.

[4] Y.-J. Chiu, X.-Y. Li, Y. C. Chen, S. R. Jian, C. H. Yang, and I. H. Lin, "Three methods for studying coupled vibration in a multi flexible disk rotor system," *Journal of Mechanical Science and Technology*, vol. 31, no. 11, pp. 5219–5229, 2017.

[5] A. Wanga and X. Cheng, "Dynamic analysis and numerical experiments for balancing of the continuous single-disc and single-span rotor-bearing system," *Communications in Nonlinear Science and Numerical Simulation*, vol. 11, no. 25, pp. 66–582, 2001.

[6] S. Jia and I. Howard, "Comparison of localised spalling and crack damage from dynamic modelling of spur gear vibrations," *Mechanical Systems and Signal Processing*, vol. 20, no. 2, pp. 332–349, 2006.

[7] N. Sawalhi and R. B. Randall, "Simulating gear and bearing interactions in the presence of faults: part I. The combined gear bearing dynamic model and the simulation of localised bearing faults," *Mechanical Systems and Signal Processing*, vol. 2, no. 21, pp. 195–211, 2008.

[8] D. Jianxiong, J. Tang, and Z. Hu, "Dynamic characteristics of the face gear transmission system based on arotor-shaft-bearing model with multiple nodes," *International Journal of Non-linear Mechanics*, vol. 137, no. 26, pp. 103825–103830, 2021.

[9] P. P. Hanmant and B. Pratiher, "Large deflection model for rub-impact analysis in high-speed rotor-bearing system with mass unbalance," *International Journal of Non-linear Mechanics*, vol. 132, no. 32, pp. 103702–103710, 2021.

[10] A. Kahraman, H. N. Ozguven, D. R. Houser, and J. J. Zakrajsek, "Dynamic analysis of geared rotors by finite elements," *Journal of Mechanical Design*, vol. 114, no. 3, pp. 507–514, 1992.

[11] C. H. Kang, W. C. Hsu, and E. K. Lee, "Dynamic analysis of gear-rotor system with viscoelastic supports under residual shaft bow effect," *Mechanism and Machine Theory*, no. 6, pp. 334–346, 2011.

[12] S. Chen, J. Tang, Y. Li, and Z. Hu, "Rotor dynamics analysis of a double-helical gear transmission system," *Meccanica*, vol. 51, no. 1, pp. 251–268, 2016.

[13] J. R. Cho, K. Y. Jeong, M. H. Park, and N. G. Park, "Dynamic response analysis of wind turbine gearbox using simplified local tooth stiffness of internal gear system," *Journal of Computational and Nonlinear Dynamics*, vol. 10, no. 4, pp. 1–8, 2015.

[14] H. Ma and P. Xu, "Fault features analysis of cracked gear considering the effects of the extended tooth contact," *Engineering Failure Analysis*, vol. 4, no. 15, pp. 79–91, 2015.

[15] S. P. Harsha, K. Sandeep, and R. Prakash, "Nonlinear dynamic behaviors of rolling element bearings due to surface waviness," *Journal of Sound and Vibration*, vol. 272, no. 3-5, pp. 557–580, 2004.

[16] L. Yang, T. Xu, H. Xu, and Y. Wu, "Mechanical behavior of double-row tapered roller bearing under combined external loads and angular misalignment," *International Journal of Mechanical Sciences*, vol. 142-143, no. 18, pp. 561–574, 2018.

[17] K. Yan, N. Wang, Q. Zhai et al., "Theoretical and experimental investigation on the thermal characteristics of double-row

tapered roller bearings of high-speed train," *International Journal of Heat and Mass Transfer*, vol. 11, no. 16, pp. 19–30, 2015.

[18] Z. W. Wang, W. H. Zhang, Z. H. Yin, Y. Cheng, G. Huang, and H. Zou, "Effect of vehicle vibration environment of high-speed train on dynamic performance of axle box bearing," *Vehicle System Dynamics*, vol. 57, no. 4, pp. 543–563, 2019.

[19] Z. W. Wang, Y. Cheng, G. M. Mei et al., "Torsional vibration analysis of the gear transmission system of high-speed trains with wheel defects," *Proc IMechE, Part F: J Rail and Rapid Transit.*vol. 12, no. 10, pp. 25–32, 2019.

[20] G. H. Huang, N. Zhou, and W. H. Zhang, "Effect of internal dynamic excitation of the traction system on the dynamic behavior of a high-speed train," *Proceedings of the Institution of Mechanical Engineers - Part F: Journal of Rail and Rapid Transit*, vol. 230, no. 8, pp. 1899–1907, 2016.

[21] X. Zhang, J. Zhong, W. Li, and M. Bocianc, "Nonlinear dynamic analysis of high-speed gear pair with wear fault and tooth contact temperature for a wind turbine gearbox," *Mechanism and Machine Theory*, vol. 173, p. 104840, 2022.